



Challenging AQP4 druggability for NMO-IgG antibody binding using molecular dynamics and molecular interaction fields



Giuseppe Felice Mangiatordi^a, Domenico Alberga^{b,c}, Lydia Siragusa^d, Laura Goracci^e, Gianluca Lattanzi^{b,c}, Orazio Nicolotti^{a,c,*}

^a Dipartimento di Farmacia – Scienze del Farmaco, Via Orabona, 4, Università di Bari “Aldo Moro”, Bari, Italy

^b Dipartimento Interateneo di Fisica “M. Merlin”, Università di Bari “Aldo Moro” and INFN, Via E. Orabona, 4, I-70126 Bari, Italy

^c Centro Ricerche TIRES, University of Bari “Aldo Moro”, Via Amendola 173, I-70126 Bari, Italy

^d Molecular Discovery Limited, 215 Marsh Road, Pinner, Middlesex, London HA5 5NE, UK

^e Department of Chemistry, Biology and Biotechnology, University of Perugia, 06123 Perugia, Italy

ARTICLE INFO

Article history:

Received 18 November 2014

Received in revised form 26 February 2015

Accepted 23 March 2015

Available online 31 March 2015

Keywords:

Molecular dynamics

Molecular interaction fields

Aquaporins

Druggability

Molecular docking

ABSTRACT

Neuromyelitis optica (NMO) is a multiple sclerosis-like immunopathology disease affecting optic nerves and the spinal cord. Its pathological hallmark is the deposition of a typical immunoglobulin, called NMO-IgG, against the water channel Aquaporin-4 (AQP4). Preventing NMO-IgG binding would represent a valuable molecular strategy for a focused NMO therapy. The recent observation that aspartate in position 69 (D69) is determinant for the formation of NMO-IgG epitopes prompted us to carry out intensive Molecular Dynamics (MD) studies on a number of single-point AQP4 mutants. Here, we report a domino effect originating from the point mutation at position 69: we find that the side chain of T62 is reoriented far from its expected position leaning on the lumen of the pore. More importantly, the strength of the H-bond interaction between L53 and T56, at the basis of the loop A, is substantially weakened. These events represent important pieces of a clear-cut mechanistic rationale behind the failure of the NMO-IgG binding, while the water channel function as well as the propensity to aggregate into OAPs remains unaltered. The molecular interaction fields (MIF)-based analysis of cavities complemented MD findings indicating a putative binding site comprising the same residues determining epitope reorganization. In this respect, docking studies unveiled an intriguing perspective to address the future design of small drug-like compounds against NMO. In agreement with recent experimental observations, the present study is the first computational attempt to elucidate NMO-IgG binding at the molecular level, as well as a first effort toward a less elusive AQP4 druggability.

© 2015 Elsevier B.V. All rights reserved.

1. Introduction

As a family of pore-forming membrane proteins, aquaporins (AQPs) allow the fast and selective flux of water and other small solutes through biological membranes [1–6]. Among the 13 homologous aquaporins identified so far, Aquaporin-4 (AQP4) has attracted increasing interest in the last years. Indeed, it plays a critical role in deafness [7, 8], in the formation of brain edema [9,10] and is the target antigen of IgG autoantibodies in the neuroinflammatory demyelinating disease Neuromyelitis Optica (NMO) [11,12], a multiple sclerosis-like disorder that predominantly features immunopathology in the optic nerves and the spinal cord [13]. The binding of serum autoantibody (NMO-IgG) to AQP4 enhances the perivascular inflammation characteristic of NMO and induces breakdown of the blood–brain barrier. The presence

of NMO-IgG against AQP4 is presently considered a signal for the onset of NMO, being detected in about 75% of patients showing such a disabling disorder [13]. AQP4 is expressed at the plasma membrane in astrocytes, in the central nervous system, and in various peripheral organs such as skeletal muscle and kidney [14,15]. From a structural point of view, it is characterized by six transmembrane helices forming a water selective pore in the center of the molecule [16].

Two different human isoforms of AQP4 have been identified so far, namely M1 (32 kDa) and M23 (30 kDa). They share identical extracellular domain residues but M1 comprises 22 more amino acids at the cytoplasmic N terminus [17,18]. These isoforms are organized in the membrane as heterotetramers, which can, in turn, aggregate to form structures known as Orthogonal Arrays of Particles (OAPs) of different sizes [19–23]. Notably, M23 is the OAP-forming isoform while it has been observed that a homotetramer of M1 is unable to form OAPs. In other words, variously sized OAPs can be observed depending on the ratio at which the two isoforms are expressed [20]. Importantly, it has been shown that conformational changes at the level of the extracellular

* Corresponding author. Tel.: +39 080 5442551.

E-mail address: orazio.nicolotti@uniba.it (O. Nicolotti).

loops A, C and E might be of relevance for the adoption of a correct epitope molecular conformation [24].

In this respect, a coauthored recent work [25] has shown that the mutation of an aspartate in position 69 (D69) impairs the binding between AQP4 and NMO-IgG leaving the water channel function unaltered as well as the formation of the OAPs. Based on 20 ns MD simulations, we speculated that the replacement of D69 with a histidine was responsible for an increased mobility of loop A, with the consequent disruption of the conformational epitopes. Building on this hypothesis, in the present work we have extended the previous MD simulations to 100 ns-long trajectories for the AQP4 tetramer of wild type (WT) and each mutated form (MT). The longer simulation time allowed us to identify the reorientation of the side chain of T62 as a key element for epitope recognition and thus for NMO-IgG binding. In recent years molecular dynamics (MD) simulations proved effective to obtain important structural and mechanistic insights into the water transport of aquaporins [26–33]. Here, we employ the same technique to obtain some insight on NMO-IgG epitope reorganization. In addition, the need to elucidate the druggability of AQP4 has prompted us to use the GRID molecular interactions fields (MIFs) [34]. We have sampled the AQP4 surface in the search for appropriately sized cavities acting as putative binding sites for protein–ligand recognition. In particular, the AQP4 druggability has been assessed with respect to known targetable proteins. Finally, induced fit docking simulations were successfully carried out on three compounds that are, to date, the only ones demonstrating an appreciable inhibition of NMO-IgG binding to AQP4 in NMO patient sera.

2. Materials and methods

2.1. From X-ray structure to model system preparation

The starting structure of AQP4 was obtained from the Protein Data Bank (PDB), entry 3GD8 [16]. The obtained crystal was first pretreated using the protein preparation module available from the Schrödinger Suite 2013 [35] which enables to add missing hydrogen atoms and to determine the optimal protonation states for histidine residues. The simulation system was built as follows. A $120 \times 120 \text{ \AA}$ [2] POPC (1-palmitoyl,2-oleoyl-sn-glycero-3-phosphocholine) bilayer patch was first built using the membrane plugin of VMD (Visual Molecular Dynamics) [36], with the membrane normal along the z-axis. A tetramer of AQP4 was then embedded in this bilayer and lipid molecules within 0.8 \AA of heavy atoms of the protein were removed. To neutralize the system, 23 Na^+ and 19 Cl^- ions were added using the VMD's "autoionize" plugin, generating a 100 mM ionic concentration and a final system of 135,833 atoms (number computed for WT). Both mutated and WT protein structures were incorporated into a periodic box of TIP3P water molecules [37] extended by 18 \AA in each direction from all protein atoms using the "solvate" plugin of VMD. In the $\text{D}^{69\text{H}}$ mutated protein, two tautomeric states for histidine are possible. In the first ($\text{D}^{69\text{HSD}}$), the hydrogen atom is bonded to the carbon δ of H69, while in the second ($\text{D}^{69\text{HSE}}$) the hydrogen atom is bonded to the carbon ϵ of H69. In our investigation, the tautomeric state of histidine 69 was univocally assigned on the basis of the hydrogen bond network predictable from the X-ray of AQP0 (PDB codes 1YMG and 2B6P). Indeed, this was the rationale inspiring the mutations at position 69 [25] since NMO-IgGs did not recognize chimeras made by AQP0 transmembrane domains [24]. The pretreatment of such crystals using the protein preparation module available from the Schrödinger Suite 2013 [35] returned hydrogen bonded to carbon δ of H69. So, hereafter $\text{D}^{69\text{H}}$ will indicate a mutation involving hydrogen bonded to carbon δ of H69. However, since tautomers can interconvert under physiological conditions and play very different actions, we decided to build also the $\text{D}^{69\text{HSE}}$ system, as a control MD simulation. The obtained data are shown in the Supporting Information (Fig. S1).

2.2. Molecular dynamics simulations

All MD simulations were performed using NAMD 2.9 [38] and the CHARMM27 force field [39]. The full system was minimized to remove steric clashes in the initial geometry and gradually heated up to 310 K within 500 ps of MD. The SHAKE algorithm was employed to constrain all R–H bonds. Periodic boundary conditions were applied in all directions. A non-bonded cut-off of 12 \AA was used, whereas the Particle-Mesh-Ewald (PME) [40] was employed to include the contributions of long-range interactions. All simulations were performed in an isothermal–isobaric ensemble (1 atm, 310 K) with a Nosè–Hoover Langevin barostat [41,42] (oscillation period 200 fs, decay coefficient 100 fs) and a Langevin thermostat [43] (damping coefficient 1 ps^{-1}). The time step was set to 2 fs, and coordinates were saved every 1000 steps (2 ps). For all the considered systems, the equilibration of the structure required less than 5 ns and, thus, the first 5 ns were removed from the analysis of the obtained 100 ns of trajectory. All simulations were performed on the FERMI supercomputer at CINECA, Italy.

2.3. Calculation of the osmotic permeability

The osmotic permeability (p_f) matrix was calculated in the framework of the theory proposed by Zhu et al. [44]. The trajectory was subdivided in time intervals of 5 ns each, and the p_f was calculated for each monomer and each time interval.

The first step consisted in the computation of the variable dn :

$$dn = \sum_{i \in S(t)} dz_i/L$$

where dz_i is the displacement of the water molecule i along the z direction within the time interval dt and $S(t)$ is the set of water molecules inside the channel of length L at time t .

Considering $n(t)$ as the integral of dn over time, the total diffusion coefficient D_n is given by the mean-square displacement as follows:

$$\langle n^2(t) \rangle = 2D_n t + C$$

where C is a constant.

Finally the osmotic permeability was computed as:

$$P_f = v_w D_n$$

where, v_w is the average volume occupied by a single water molecule.

2.4. Identification of cavities

The *FLAPsite* [45–47] algorithm was used for the identification of cavities within the AQP4 crystal structure (PDB entry: 3GD8). The procedure started by embedding the target protein into a grid with a spatial resolution of 1.0 \AA . Two GRID [34] probes were used by the detection routine: the GRID [34] H probe (shape) to identify pocket points and the DRY probe (hydrophobic) for buriedness calculation prioritizing hydrophobic cavities. Once all pockets points were identified by H probe, the next step focused on grid points located within a distance of 4 \AA from the closest protein atom, excluding protein surface points. For the remaining points, a buriedness-index was calculated. The buriedness-index was also weighted by the hydrophobicity computed using the GRID hydrophobic DRY probe. Points with a buriedness-index lower than a pre-determined threshold were discarded. The remaining points were processed by two morphological operations, namely *erosion* to remove small anomalies (decreasing the size of the cavity) and *dilation* to fill holes and connect areas (increasing the size of the cavity). By using the GRID hydrophobic probe (DRY), hydrophobic interactions were calculated for each cavity. Cavities showing favorable

hydrophobic interactions were prioritized, since they usually bind drug molecules.

2.5. Druggability assessment

We collected a reference dataset containing 43 target structures defined as ‘druggable’ by Cheng et al. [48]. The cavities for each target were detected by the FLAPsite tool [45,46]. Volsurf [49,50] descriptors were used to characterize either the AQP4 cavity close to the loop A or each pocket in the reference druggable target dataset. Volume, surface, rugosity, globularity, hydrophobicity, hydrophilicity and charged residues descriptors were calculated. *Pocket volume* and *surface* represent the water-excluded volume and the accessible surface respectively, traced out by the GRID OH2 probe (water probe). Rugosity and globularity represent the presence of wrinkles or creases on the pocket surface and the degree of sphericity of the pocket, respectively. Hydrophobicity and hydrophilicity were quantified using the GRID probes DRY and OH2 respectively. The hydrophobic probe is used to mimic the pocket attractive hydrophobic interactions, while the water probe is used to mimic solvation–desolvation processes. GRID probes N1+ and O− are instead suitable probes used to detect charge–charge electrostatic interactions but also polar interactions generated by pocket residues. A comparative analysis of the AQP4 cavity against the well-known druggable active sites reference dataset was performed by plotting distributions of the corresponding chemical–physical properties.

2.6. Docking studies

Flexible receptor docking studies were performed using a multi-stage induced fit docking protocol (IFD) available from the Schrödinger Suite 2013 [35]. A cubic docking grid centered on the centroid of residues T62, D69 and T56 and having a side equal to 26 Å was used. In the first stage, the van der Waals radii of the protein and the ligand were scaled by a factor of 0.5 and ligands were docked using the default Glide SP mode. Subsequently, prime was used to predict and optimize the selected protein side chains. The poses were scored and filtered, and finally ligands were redocked using the Glide SP mode and scored.

3. Results

All results shown in the present section were obtained analyzing the calculated MD trajectories (95 ns at 310 K after 5 ns of equilibration for each considered system). Beyond the wild type (WT), three different

engineered mutants were investigated: D⁶⁹E, D⁶⁹H and M⁷⁰V. The latter was employed as a negative control, since such mutation is known not to affect the NMO-IgG epitope unlike the other MTs [25]. A synoptic view is reported in Fig. 1.

First, we report the analysis of distances of alpha carbon atoms averaged among the four monomers (C- α_{AV}) in order to investigate the occurrence of possible conformational changes in the nearby of the considered mutations. Second, we analyze the differences between WT and MTs in terms of H-bond interactions during the simulation. Third, we show the obtained osmotic permeabilities for the WT and all the considered MTs. Fourth, we describe the predicted AQP4 cavity, pointing out its putative role as a binding site.

3.1. C- α_{AV} distances

As shown in Fig. 2, the AQP4 tetramer is axially-symmetric with respect to the z-axis passing through the center of the system. As a result, the distances of a given residue in the 4 monomers from the z-axis are expected to be almost equal. Keeping this in mind, the global effect of the mutations was evaluated by averaging data over the four monomers. In particular, the distance between the C-alpha of a given residue in a given monomer vs. its specular symmetric (i.e. monomer A vs. B and monomer C vs. D, see Fig. 2) was computed. A value averaged along the obtained MD trajectory was considered for both occurrences (monomer A vs. monomer B and monomer C vs. monomer D, see Fig. 2). Finally, the two obtained values were further averaged in order to have a single parameter for each residue, hereafter named C- α_{AV} .

As shown in Fig. 3a, C- α_{AV} distances for all MTs and the WT do overlap over the entire protein sequence, including the extracellular loops. Interestingly, an exception is represented by few residues just upstream the mutation, in particular from residue G60 to residue L66, a region that is part of the extracellular loop A. This becomes even clearer in Fig. 3b where a zoomed view is shown. The uncertainties related to C-alpha distances were calculated by the block averaging method (see the section “statistical analysis” in the supporting information for details). In particular, threonine at position 62 (hereafter referred to as T62) is the residue showing the largest difference when comparing C- α_{AV} of WT and MTs. In other words, the computed C- α_{AV} values suggest a sort of “domino effect” [51] where the substitution of a single residue in position 69 induces a substantial modification of the conformation of other residues upstream the mutation.

Focusing our attention on residue T62, the C- α_{AV} values closest to WT (31.37 ± 0.66 Å) are exhibited by D⁶⁹E (31.39 ± 1.73 Å) and M⁷⁰V

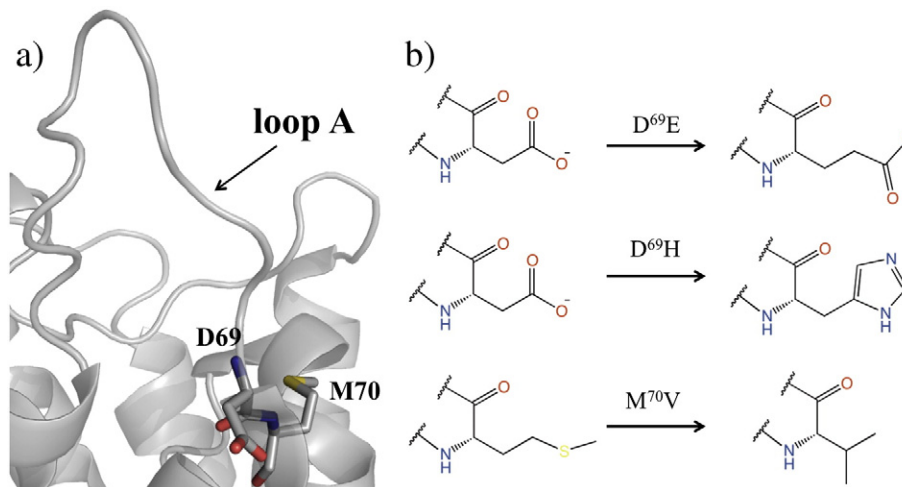


Fig. 1. Sketches of the residues involved in the considered mutations. Note that D69 and M70 are the first residues of the trans-membrane region downstream of loop A.

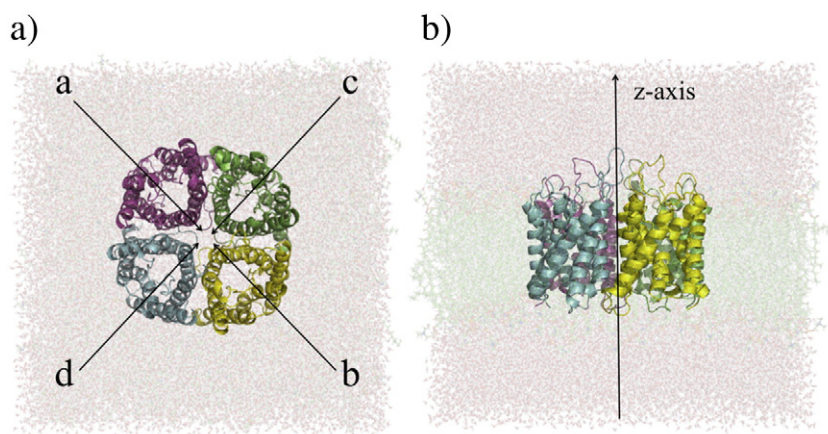


Fig. 2. a) Top view and b) lateral view of the investigated systems. Water molecules and the membrane bilayer are rendered as sticks while the AQP4 tetramer is shown in cartoon representation.

(31.45 ± 0.65 Å), while a substantial difference is shown by D⁶⁹H (34.73 ± 0.47 Å), being such C α_{AV} value > 3 Å compared to WT. Such trend, based on averaged values, is also confirmed when the two computed C-alpha distances (monomer A vs. B and monomer C vs. D) are considered separately. Regarding residue T62, for instance, both data for WT (29.86 ± 0.54 and 32.88 ± 0.38) are lower than those obtained for D⁶⁹H (35.22 ± 0.36 and 34.24 ± 0.30). The reported error bars clearly demonstrate the statistical significance of the observed differences. These findings are in agreement with our recent work [25] where we first hypothesized that the effect of the point mutation in 69 is transferred to residues upstream the mutation, including T62. We do not report significant differences in the C-alpha_{AV} distances

between WT and D69E. However this does not imply that the D69E mutation has no effect, as will be explained below.

As shown in Fig. 4a, data taken from the trajectory of WT display a Gaussian distribution. In particular, most of the obtained MD snapshots show C-alpha distances in a range of 30–34 Å. The distribution function computed for the D⁶⁹E mutant provided a wealth of additional information with respect to the mere analysis of the C-alpha_{AV}. Despite the fact that C-alpha_{AV} values computed for T62 of WT and D⁶⁹E are almost equal, their corresponding distribution functions are strongly different. In fact, a bimodal distribution can be detected only for D⁶⁹E thus indicating the occurrence of two dominant conformational states. The first one (hereafter referred to as D⁶⁹E(1)), missing in WT, discloses a peak around 21 Å whereas the second one (D⁶⁹E(2)) is shifted to larger values (peak around 36 Å) with respect to WT. More importantly, this second and more populated state shows a nice overlap with that of D⁶⁹H, the mutant showing the largest difference in terms of C-alpha_{AV} compared to WT. On the other hand, M⁷⁰V does not display any appreciable difference compared to WT, thus confirming the indications obtained by the analysis of the sole C-alpha_{AV}.

For the sake of completeness, Fig. 4b shows the computed cumulative probabilities for WT and all the considered mutants: it is clear that the curves computed for D⁶⁹E(2) and D⁶⁹H do overlap and strongly diverge from WT (shift of about 4 Å). In other words, the trajectories of D⁶⁹H and D⁶⁹E suggest that a mutation in position 69 may turn away T62 residues and induce a significant diversion of loops A. In this respect, it is worth saying that a value of distance < 27 Å is still found in about 15% of the WT and M⁷⁰V snapshots while it does not occur in D⁶⁹E(2) and D⁶⁹H.

We notice also that the conformational state D⁶⁹E(1) results from the interaction, occurring at the monomer D, between K64, positively charged and belonging to loop A, and the negatively charged mutated residue, namely E69. This event is quite persistent for about 35 ns and leads to the closure of loop A and, consequently, to a strong decrease of the C-alpha distance (monomer A vs. monomer B) computed for T62. For further information regarding the D⁶⁹E(1) state the interested reader is referred to Figs. S7 and S8 in the Supporting Information.

3.2. Analysis of hydrogen bond interactions

To further investigate the diverse behaviors of WT and MTs, we conducted a deep analysis of the hydrogen bond interactions occurring in the tetramer within the simulated trajectories. Interestingly, the sole appreciable difference was observed for threonine at position 56 (T56), a residue belonging to loop A. Such finding supports again the hypothesis that this extracellular loop is under the remote control of the single point mutation at position 69. In this respect, Table 1 reports the rate of

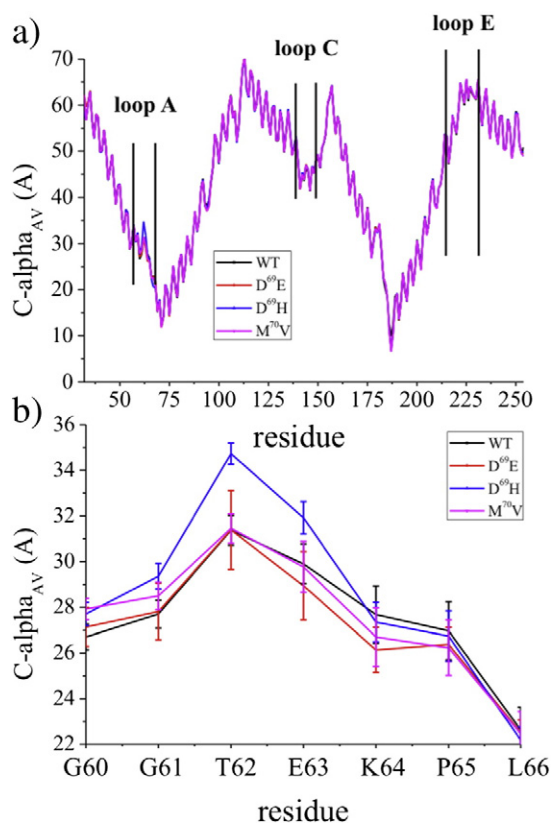


Fig. 3. a) C-alpha_{AV} values (Å) computed for all residues of the investigated systems. b) Zoomed figure showing C-alpha_{AV} data and corresponding error bars (Å) computed for residues belonging to a portion of loop A (from residue G60 to residue L66).

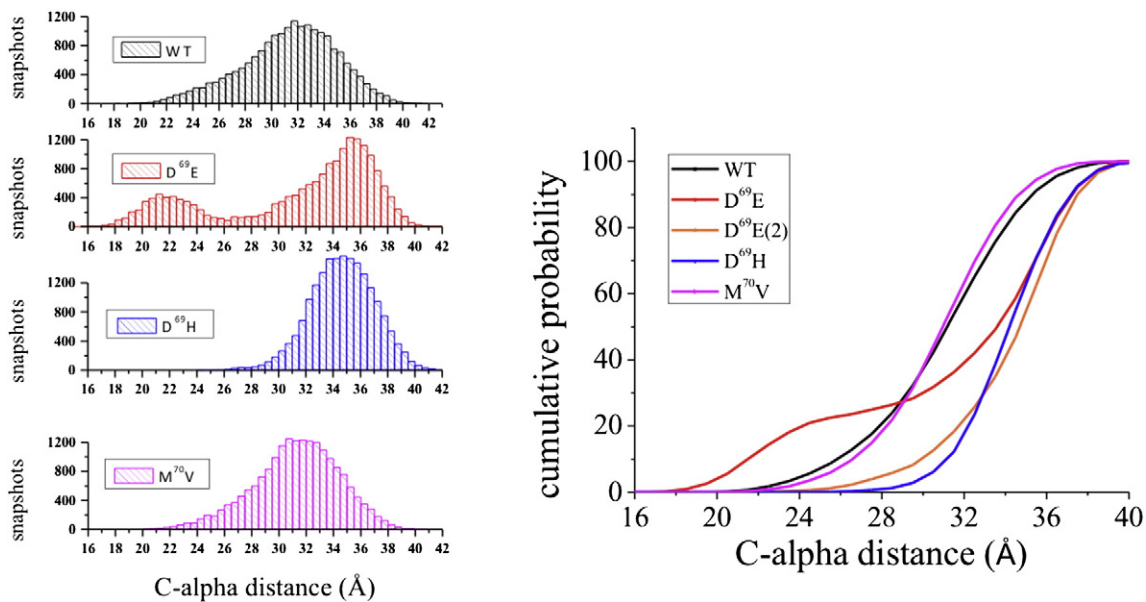


Fig. 4. Distance distribution function (left) and cumulative probability (right) of C-alpha distances computed for residue T62. D^{69E}(2) refers to data computed for the second conformational state of D^{69E}.

occurrence (%) of the hydrogen bond established between the side chain of T62 (donor) and the backbone of Leucine in position 53 (L53 – acceptor) during the entire analyzed trajectories.

The values in Table 1 indicate the percentage of frames in which the hydrogen bond is formed, using as thresholds a distance atom acceptor (AA)–atom donor (AD) equal to 3 Å and an angle AD–H–AA equal to 160°. In all considered MTs, such interaction occurs less frequently with respect to WT and, again, the major difference is observed in the case of D^{69E} and D^{69H}, being the corresponding percentages (22.72% and 11.00% respectively) lower than WT (32.40%). On the other side, data obtained from the trajectory of M70V (27.24%) are closer to WT. It is worth noting that such percentage was computed by assuming that the four monomers behave independently, so that for each system (i.e. WT and MTs) a trajectory equal to 95 ns × 4 was considered. Nevertheless, the robustness of these data is confirmed by the evidence that the observed differences also occur considering each monomer separately. Regarding D^{69H}, for instance, the values obtained for monomers A (10.62%), B (14.16%), C (10.16%) and D (9.06%) are all lower with respect to those computed for WT, being equal to 31.96% (monomer A), 39.22% (B), 20.76% (C) and 37.64% (D). For the sake of clarity, representative MD snapshots are shown in Fig. 5 to indicate the residues engaged in hydrogen bond interactions for the WT and all MTs.

A further proof reinforcing the solidity of these data is given by the time dependent evolutions of the distance between atom acceptor (oxygen atom of the hydroxyl group of T56) and atom donor (oxygen atom of the carbonyl of the backbone of L53). Fig. S2 (see supporting information) shows the results taking into account all the monomers of WT and D^{69H}: frames showing distances compatible with the H-bond interactions are much less frequent in all the monomers of D^{69H} with respect to WT and the H-bond interaction, when it occurs, persists only for a few nanoseconds. In summary, the analysis of the hydrogen

bond interactions indicates that the conformational modification of the loop A, determined by the mutation at position 69, could be the result of the weakening of an interaction involving the residues T56 and L53.

3.3. Computation of the osmotic permeability

In a previous study [26], we found that two different gating mechanisms can exist inside the water pore of WT. One is associated with the well-known selectivity filter (SF) on the extracellular side (residues H201 and R216); the other to the spontaneous reorientation of the imidazole ring of a histidine from loop B (H95) enabling an H-bond interaction with a cysteine belonging to the loop D (C178) at the cytoplasmic end (CE). Notably, two different local constriction indicators (LCIs) were defined: 1) d_{SF} , which measures the distance between the nitrogen hydrogen bond (HB)-acceptor atom of H201 and the closer terminal nitrogen atom of R216 at the selectivity filter (SF); 2) d_{CE} , which measures the distance between the nitrogen HB-acceptor atom of H95 and the sulfur atom of C178 at the CE. Based on the time evolution of the LCIs, 4 different representative segments of trajectory were selected and for each of them the total osmotic permeability was computed in order to evaluate how it can be related to the different states, namely open/open, open/closed, closed/open and closed/closed (following the scheme SF/CE).

Herein, we extend this analysis to all the investigated MTs. However, as for WT, variations at the level of SF are quite rare and even when they occur, the closed state rapidly switches back to the open one. For the sake of simplicity, the states herein considered were therefore those open/open and open/closed. The results are shown in Table 2 while the time dependent evolutions of d_{CE} for all the considered systems are given in Figs. S3–S6 (see Supporting Information).

In all the considered systems, the gating mechanism at the cytoplasmic end affects heavily the permeability of the pore, with a decrease of p_f resulting from the closure of CE, in the order of about 70%. Furthermore, the values computed for all the MTs, considering both open and closed states, are in good agreement with those obtained for WT. In other words, these data suggest that although the mutation D69 can strongly affect the epitope formation, it does not have any effect in terms of AQP4 water channel properties. Remarkably, these results are in full agreement with recent experimental observations [25].

Table 1

Occupancy (%) of the H-bond (donor–acceptor) occurring between the side chain of T62 and the main chain of L53 in the considered systems. An atom donor (AD)–atom acceptor (AA) distance equal to 3 Å and an angle AD–H–AA equal to 160° were used as thresholds to define the presence of the H-bond.

H-bond	WT	D ^{69E}	D ^{69H}	M ^{70V}
T56 _{SIDE} –L53 _{BACKBONE}	32.40	22.72	11.00	27.24

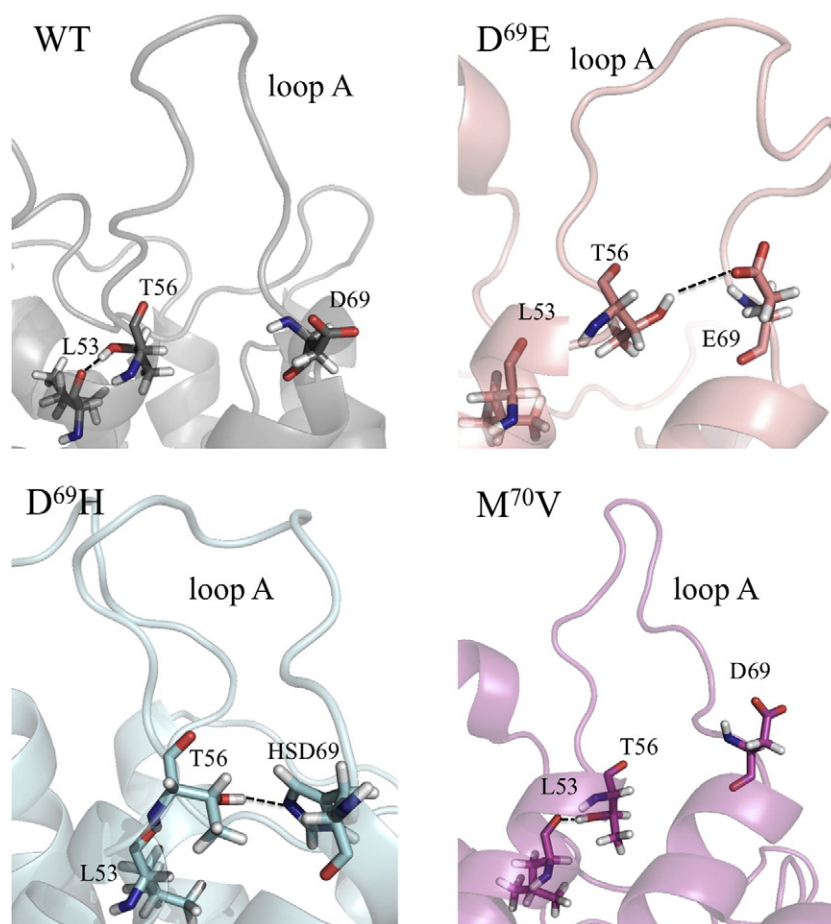


Fig. 5. Selected frames showing the H-bond interaction involving the side chain of T56 and the backbone of L53 in WT and M⁷⁰V and the putative interaction between T56 and E69 present in D⁶⁹E and between T56 and H69 present in D⁶⁹H.

3.4. Analysis of cavities

With the aim to target the AQP4 protein with small-molecules and look for potentially active blockers, we searched for all the potential cavities that are present in the AQP4 crystal structure (PDB code 3GD8) [16] with the FLAPsite algorithm. As shown in Fig. 6, the sole cavity predicted is located in the neighborhood of loop A. This observation suggests that this region would be suitable for accommodating small-molecules, therapeutically important, to prevent antibody binding.

Further investigations of the potential druggability of this site were performed using molecular interaction fields (MIF)-based descriptors. As shown in Fig. 7a, the AQP4 cavity (blue dot) falls in the most populated range of volume, surface, rugosity, and globularity distributions of druggable active sites dataset made of 43 X-ray solved pharmaceutically relevant targets [48]. Furthermore, the computation of the interaction descriptors (hydrophobic, hydrophilic and charge–charge/polar interactions) revealed that the AQP4 cavity interaction values were again

in the same range of the reference druggable dataset, falling in the maximum distribution range (see Fig. 7b).

4. Discussion

Collectively, our results indicate that D69 is a key element for the remote control of the loop A conformation of AQP4 and, more specifically, for pushing residue T62 in or out of the lumen pore. The analysis of the 95 ns-long trajectories of WT, D⁶⁹E, D⁶⁹H and M⁷⁰V suggest that substantial modifications at the level of loop A with respect to WT can be

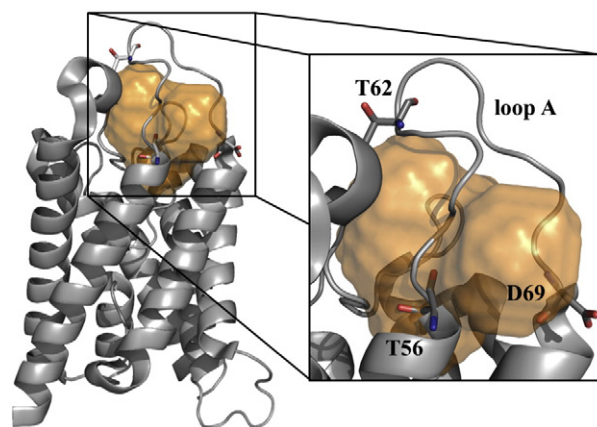


Fig. 6. Cavity identified in the AQP4 crystal structure (PDB entry: 3GD8) by the FLAPsite algorithm.

Table 2

Osmotic permeabilities (p_f) computed for WT and all MT forms of the representative segments of the trajectory corresponding to different states (open and closed) of the CE region. All data are reported in 10^{-14} cm³/s unit.

System	Status (CE)	
	Open	Closed
WT	9.5 ± 2.1	2.5 ± 0.9
D ⁶⁹ E	8.7 ± 2.5	2.3 ± 0.9
D ⁶⁹ H	8.2 ± 3.2	2.6 ± 1.8
M ⁷⁰ V	11.8 ± 2.1	2.1 ± 0.9

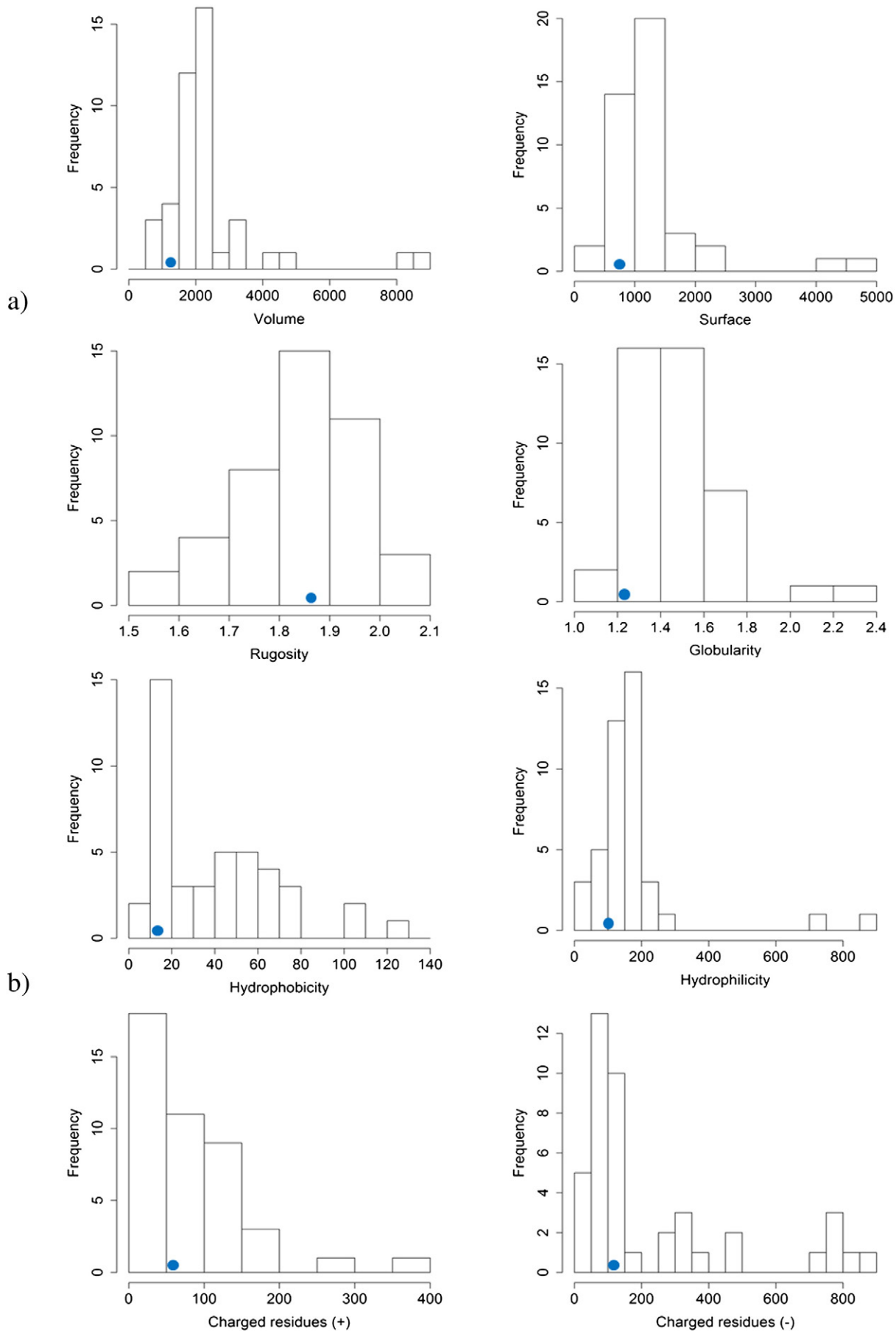


Fig. 7. Distributions of the Volsurf: (a) size and shape and (b) interaction descriptors for the active sites of the druggable reference set and position of AQP4 cavity (blue dots).

detected only for two MTs, namely D⁶⁹E and D⁶⁹H. On the other side, the analysis of the computed osmotic permeabilities does not return any appreciable difference when comparing WT and MTs. These observations match recent experimental findings whereby the considered mutants do not affect AQP4 water channel properties [25]. The mutation of D69 has instead dramatic effects on all NMO-IgG epitopes. As experimentally observed, the NMO-IgG binding is hampered mainly when the aspartate at position 69 is replaced by histidine. No effects on NMO-IgG binding were instead observed for the M⁷⁰V case. Actually, our MD studies confirm a substantial overlap of the M⁷⁰V mutant with WT, with respect to the conformations assumed by loop A. The good match between theoretical and experimental data allows us to speculate on the features of the conformational epitope.

More specifically, it can be reasonably assumed that, in WT and M⁷⁰V, NMO-IgG binding can be ensured by a specific conformation of T62 that is able to protrude inside the central pore lumen in a kind of “closed conformation”, which is forbidden to D⁶⁹E and D⁶⁹H having a higher propensity to equilibrate in a kind of “open conformation”, thus disrupting the conformational epitope.

Moreover, the analysis of the H-bond interactions confirms the involvement of the loop A. Indeed, a substantial difference in terms of H-bond occurrence was observed between WT and the MTs. This interaction involves the hydroxyl group of T56 acting as H-bond donor and the carbonyl group of the backbone of L53 acting as H-bond acceptor. It should be noted that T56 belongs to loop A while L53 is part of the first transmembrane segment, named TM1. Furthermore, although the mutated residue is at position 69, T56 is located at the base of the loop A, having an adjacent residue belonging to a transmembrane region. As clearly shown in Fig. 5, the effect of mutations at position 69 is that of rotating the sidechain of T56 with the consequent disruption of the interaction T56_{SIDE}–L53_{MAIN} to favor the hydrogen bond engagement with the side chain of the glutamate or of the histidine in position 69. This becomes even clearer if we consider the average distances computed from the center of mass of the side chain, hereafter termed as CoM_{AV}, instead of C_{alpha}_{AV}. In fact, considering the mutated residue D⁶⁹H, we observe an increase in the CoM_{AV} value >3 Å when compared to WT (14.74 Å vs. 11.50 Å), thus confirming a net trend for MTs to place the mutated residue towards T56.

Taken together, these results indicate that the effect of the D69 mutation consists in altering the loop A conformation and in particular the spatial position of T62. Interestingly, here we first report that such a conformational modification is the result of upstream weakening of the hydrogen bond interaction T56_{SIDE}–L53_{BACKBONE}. This event is, in turn, due to the higher propensity of the side chain of the mutated residue at position 69 to attract the side chain of T56. As mentioned above, our herein presented hypothesis is supported by experimental literature [25,52]. In particular Miyazaki et al. [52] conclude not only that the “replacement of loop A drastically reduces the binding of the antibodies to human AQP4” but also that, among the other residues, “T62 and/or L64 are involved in the epitope of the monoclonal antibodies”. The epitope molecular features are recognition elements essential to address the design of modulators of the NMO-IgG AQP4 binding. This is a topic of extreme interest being AQP4 druggability [53] yet to demonstrate. It is well known that druggability studies are indeed important to evaluate the likelihood that small drug-like molecules bind a given target [54,55]. Indeed, an obstacle in the development of efficient AQP4 blockers might be due to the extreme difficulty to identify cavities that would be large enough to accommodate possible drug-like small-molecules. In this respect, we first considered the chance to detect cavities in the AQP4 surface by using FLAPsite and then we assessed their suitability for the binding of small-molecules by comparison with a dataset of druggable active sites [48]. Using the FLAPsite algorithm [34] the entire surface of the AQP4 crystal structure (PDB entry: 3GD8) was scanned looking for suitable molecular cavities. We found only a putative binding site at the top of the channel located

close to loop A (see Fig. 6). The druggability of such potential binding site was, thus, assessed by a knowledge-based approach. Using MIF-based descriptors, the chemical–physical properties of the AQP4 cavity were compared with those of well-known druggable active sites. As shown in Fig. 7, the chemical–physical properties of the AQP4 cavity are in the same range of the druggable reference dataset. More importantly, the AQP4 cavity intercepted, among the distribution ranges of the size, shape and interaction descriptors, the highest populated bins. Such knowledge-based observation discloses an intriguing scenario and, to some extent, prompts us to hypothesize that AQP4 could be considered as a druggable target. Interestingly, MD studies and experimental evidences univocally indicate that loop A is important for NMO-IgG binding; in addition the FLAPsite algorithm suggests that a binding pocket for drug-like small-molecules is at the base of this loop. To the best of our knowledge, the sole small-molecules ever demonstrating an appreciable inhibition of NMO-IgG binding to AQP4 in NMO patient sera are arbidol, tamarixetin and berbamine (see Fig. 8). In this respect, we refer to the paper of Tradtrantip et al. [56] reporting, for these three compounds, classical docking simulations focused into a region flanked by residues at the base of loop A (namely I57, N58 and V68). Retrospectively, this region discloses a substantial overlap with the AQP4 cavity identified by FLAPsite. On the basis of MD studies indicating that loop A experiences a conformational change after mutating the aspartate at position 69 (whose main effect was that of preventing NMO-IgG binding without affecting water permeability), we carried out induced fit docking (IFD) simulations enabling the ligand to determine conformational changes of the residues forming the AQP4 cavity, designated as a receptor active site.

The top scoring poses obtained for arbidol, tamarixetin and berbamine are shown in Fig. 8. Importantly, the lowest-energy docked conformations were found at the loop A and almost completely inside our AQP4 cavity. We notice that a very large docking box (side equal to 26 Å, by default) was used in order to take into account possible interactions with other extracellular loops. Consistently with the investigation of Tradtrantip et al. [56] the compounds projected toward a hydrophobic cavity between the two transmembrane regions connected by loop A. However, here, the use of an IFD protocol allowed us to obtain several important additional clues. Arbidol and tamarixetin establish a strong H-bond interaction with D69, whose side chain changes its conformation with respect to the crystal (see zoom in Fig. 8). Along with D69, also L72 and W59 change their conformation in order to maximize a hydrophobic and an aromatic–aromatic interaction respectively. Moreover, both ligands engage an H-bond interaction with the backbone of W59 whereas in the case of tamarixetin an additional interaction with N58 is also found. In this respect, IFD calculations enrich the observations coming from MD and FLAPsite, complementing those molecular analyses. Taken together, our study indicates that the identified AQP4 cavity has the desirable physico-chemical profile as well as the suitable room to bind drug-like molecules.

5. Conclusions

The present paper reports how the harmonized use of advanced biophysical and drug discovery strategies, already proved to be valuable for other aquaporins [57], allow in approaching very challenging targets as AQP4. Supported by very recent experimental observations [25,56], we suggest that the surface of loop A and, more importantly, of the residues flanking its basis forms a druggable cavity and, thus, a valuable target for the structure-based design of compounds able to inhibit NMO-IgG binding to AQP4 in NMO patients. At present, we are screening the entire Protein Data Bank searching for reliable cross-relationships with known targetable proteins with the aim to discover new NMO-IgG binding blockers. This ongoing attempt might help to address future design of small-molecule modulators and to plan rational drug repurposing strategies.

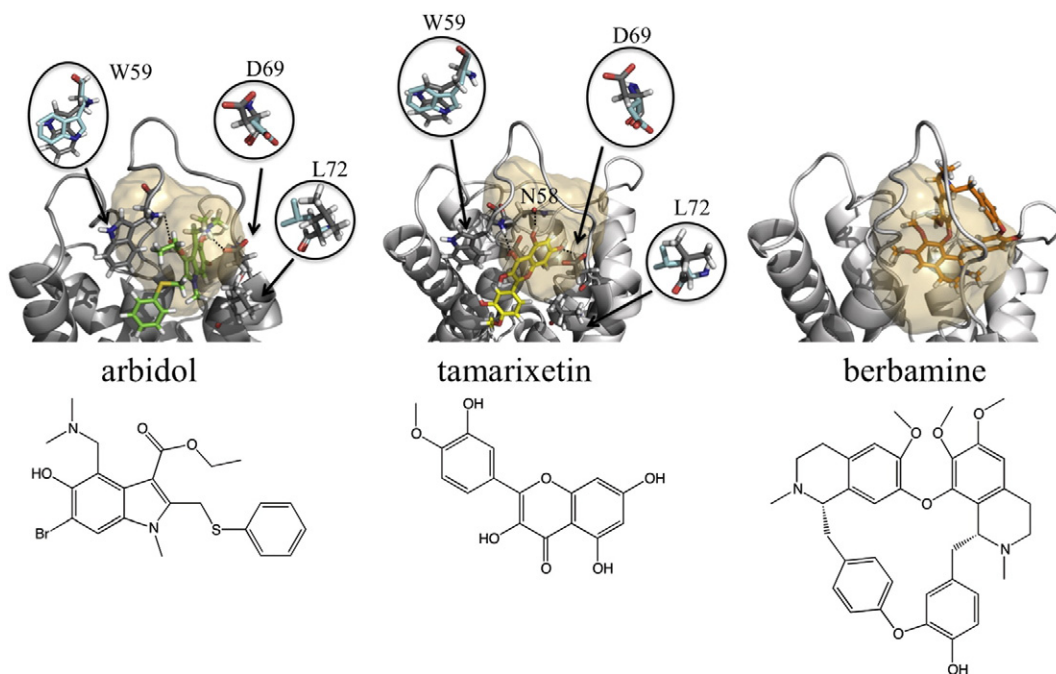


Fig. 8. Sketches and top scoring docking poses of arbidol, tamarixetin and berbamine.

Transparency Document

The Transparency document associated with this article can be found, in the online version.

Acknowledgements

This work was funded under the program FIRB (Futuro in Ricerca 2012, RBFR12SJA8_003). We acknowledge the CINECA awards nos. HP10CL5BLB-hAQP4 and HP10B4VZO7-epi-NMO under the ISCRA initiative for the availability of high-performance computing resources and support.

Appendix A. Supplementary data

Details on the statistical analysis performed to estimate the uncertainties related to our data, data from D⁶⁹HSE mutated form, time dependent evolutions of d_{CE} in all the considered systems, the time-dependence of the distance between the oxygen of the hydroxyl group of T56 (atom acceptor) and the oxygen of the carbonyl of the backbone of L53 (atom donor) in WT and D⁶⁹H and all the details about the conformational state of D⁶⁹H are given in the Supporting Information. This material is available free of charge via the Internet at <http://pubs.acs.org>. Supplementary data associated with this article can be found, in the online version, at <http://dx.doi.org/10.1016/j.bbamem.2015.03.019>.

References

- [1] S. Nielsen, E.A. Nagelhus, M. Amiry-Moghaddam, C. Bourque, P. Agre, O.P. Ottersen, Specialized membrane domains for water transport in glial cells: high-resolution immunogold cytochemistry of aquaporin-4 in rat brain, *J. Neurosci.* 17 (1997) 171–180.
- [2] M. Borgnia, S. Nielsen, A. Engel, P. Agre, Cellular and molecular biology of the aquaporin water channels, *Annu. Rev. Biochem.* 68 (1999) 425–458.
- [3] H. Sui, B.G. Han, J.K. Lee, P. Walian, B.K. Jap, Structural basis of water-specific transport through the AQP1 water channel, *Nature* 414 (2001) 872–878.
- [4] R. Sachdeva, B. Singh, Insights into structural mechanisms of gating induced regulation of aquaporins, *Prog. Biophys. Mol. Biol.* 114 (2014) 69–79.
- [5] B. Ilan, E. Tajkhorshid, K. Schulten, G.A. Voth, The mechanism of proton exclusion in aquaporin channels, *Proteins* 55 (2004) 223–228.
- [6] H. Li, H. Chen, C. Steinbronn, B. Wu, E. Beitz, T. Zeuthen, G.A. Voth, Enhancement of proton conductance by mutations of the selectivity filter of aquaporin-1, *J. Mol. Biol.* 407 (2011) 607–620.
- [7] G.P. Nicchia, R. Ficarella, A. Rossi, I. Giangreco, O. Nicolotti, A. Carotti, F. Pisani, X. Estivill, P. Gasparini, M. Svelto, A. Frigeri, D184E mutation in aquaporin-4 gene impairs water permeability and links to deafness, *Neuroscience* 197 (2011) 80–88.
- [8] J. Li, A.S. Verkman, Impaired hearing in mice lacking aquaporin-4 water channels, *J. Biol. Chem.* 276 (2001) 31233–31237.
- [9] Z. Zador, S. Stiver, V. Wang, G.T. Manley, Role of aquaporin-4 in cerebral edema and stroke, *Handb. Exp. Pharmacol.* (2009) 159–170.
- [10] M.C. Papadopoulos, A.S. Verkman, Aquaporin-4 and brain edema, *Pediatr. Nephrol. Berl. Ger.* 22 (2007) 778–784.
- [11] A.S. Verkman, Aquaporins in clinical medicine, *Annu. Rev. Med.* 63 (2012) 303–316.
- [12] M.C. Papadopoulos, J.L. Bennett, A.S. Verkman, Treatment of neuromyelitis optica: state-of-the-art and emerging therapies, *Nat. Rev. Neurol.* 10 (2014) 493–506.
- [13] V.A. Lennon, T.J. Kryzer, S.J. Pittock, A.S. Verkman, S.R. Hinson, IgG marker of optic-spinal multiple sclerosis binds to the aquaporin-4 water channel, *J. Exp. Med.* 202 (2005) 473–477.
- [14] M. Amiry-Moghaddam, O.P. Ottersen, The molecular basis of water transport in the brain, *Nat. Rev. Neurosci.* 4 (2003) 991–1001.
- [15] K. Yoneda, N. Yamamoto, K. Asai, K. Sobue, Y. Fujita, M. Fujita, M. Mase, K. Yamada, M. Nakanishi, T. Tada, Y. Miura, T. Kato, Regulation of aquaporin-4 expression in astrocytes, *Mol. Brain Res.* 89 (2001) 94–102.
- [16] J.D. Ho, R. Yeh, A. Sandstrom, I. Chorny, W.E.C. Harries, R.A. Robbins, L.J.W. Miercke, R.M. Stroud, Crystal structure of human aquaporin 4 at 1.8 Å and its mechanism of conductance, *Proc. Natl. Acad. Sci.* 106 (2009) 7437–7442.
- [17] F. Umenishi, A.S. Verkman, Isolation and functional analysis of alternative promoters in the human aquaporin-4 water channel gene, *Genomics* 50 (1998) 373–377.
- [18] B. Yang, T. Ma, A.S. Verkman, cDNA cloning, gene organization, and chromosomal localization of a human mercurial insensitive water channel evidence for distinct transcriptional units, *J. Biol. Chem.* 270 (1995) 22907–22913.
- [19] M. Tajima, J.M. Crane, A.S. Verkman, Aquaporin-4 (AQP4) associations and array dynamics probed by photobleaching and single-molecule analysis of green fluorescent protein-AQP4 chimeras, *J. Biol. Chem.* 285 (2010) 8163–8170.
- [20] B.-J. Jin, A. Rossi, A.S. Verkman, Model of aquaporin-4 supramolecular assembly in orthogonal arrays based on heterotetrameric association of M1–M23 isoforms, *Biophys. J.* 100 (2011) 2936–2945.
- [21] R. Iorio, J.P. Fryer, S.R. Hinson, P. Fallier-Becker, H. Wolburg, S.J. Pittock, V.A. Lennon, Astrocytic autoantibody of neuromyelitis optica (NMO-IgG) binds to aquaporin-4 extracellular loops, monomers, tetramers and high order arrays, *J. Autoimmun.* 40 (2013) 21–27.
- [22] A. Rossi, F. Baumgart, A.N. van Hoek, A.S. Verkman, Post-golgi supramolecular assembly of aquaporin-4 in orthogonal arrays, *Traffic Cph. Den.* 13 (2012) 43–53.
- [23] A. Rossi, T.J. Moritz, J. Ratelade, A.S. Verkman, Super-resolution imaging of aquaporin-4 orthogonal arrays of particles in cell membranes, *J. Cell Sci.* 125 (2012) 4405–4412.
- [24] F. Pisani, M. Mastrotoato, A. Rossi, G.P. Nicchia, C. Tortorella, M. Ruggieri, M. Trojano, A. Frigeri, M. Svelto, Identification of two major conformational aquaporin-4 epitopes for neuromyelitis optica autoantibody binding, *J. Biol. Chem.* 286 (2011) 9216–9224.

- [25] F. Pisani, M.G. Mola, L. Simone, S. Rosito, D. Alberga, G.F. Mangiatordi, G. Lattanzi, O. Nicolotti, A. Frigeri, M. Svelto, G.P. Nicchia, Identification of a point mutation impairing the binding between aquaporin-4 and the neuromyelitis optica autoantibodies, *J. Biol. Chem.* 289 (2014) 30578–30589.
- [26] D. Alberga, O. Nicolotti, G. Lattanzi, G.P. Nicchia, A. Frigeri, F. Pisani, V. Benfenati, G.F. Mangiatordi, A new gating site in human aquaporin-4: insights from molecular dynamics simulations, *Biochim. Biophys. Acta* 1838 (2014) 3052–3060.
- [27] L. Janosi, M. Ceccarelli, The gating mechanism of the human aquaporin 5 revealed by molecular dynamics simulations, *PLoS One* 8 (2013) e59897.
- [28] M. Hashido, A. Kidera, M. Ikeguchi, Water transport in aquaporins: osmotic permeability matrix analysis of molecular dynamics simulations, *Biophys. J.* 93 (2007) 373–385.
- [29] Y. Cui, D.A. Bastien, Water transport in human aquaporin-4: molecular dynamics (MD) simulations, *Biochem. Biophys. Res. Commun.* 412 (2011) 654–659.
- [30] Y. Wang, E. Tajkhorshid, Nitric oxide conduction by the brain aquaporin AQP4, *Proteins* 78 (2010) 661–670.
- [31] E. Tajkhorshid, P. Nollert, M.Ø. Jensen, L.J.W. Miercke, J. O'Connell, R.M. Stroud, K. Schulten, Control of the selectivity of the aquaporin water channel family by global orientational tuning, *Science* 296 (2002) 525–530.
- [32] B.L. de Groot, H. Grubmüller, Water permeation across biological membranes: mechanism and dynamics of aquaporin-1 and GlpF, *Science* 294 (2001) 2353–2357.
- [33] J.S. Hub, C. Aponte-Santamaria, H. Grubmüller, B.L. de Groot, Voltage-regulated water flux through aquaporin channels in silico, *Biophys. J.* 99 (2010) L97–L99.
- [34] P.J. Goodford, A computational procedure for determining energetically favorable binding sites on biologically important macromolecules, *J. Med. Chem.* 28 (1985) 849–857.
- [35] Schrödinger Release 2013-2: Maestro, Version 9.5, Schrödinger, LLC, New York, NY, 2013.
- [36] W. Humphrey, A. Dalke, K. Schulten, VMD: visual molecular dynamics, *J. Mol. Graph.* 14 (1996) 33–38.
- [37] W.L. Jorgensen, J. Chandrasekhar, J.D. Madura, R.W. Impey, M.L. Klein, Comparison of simple potential functions for simulating liquid water, *J. Chem. Phys.* 79 (1983) 926–935.
- [38] J.C. Phillips, R. Braun, W. Wang, J. Gumbart, E. Tajkhorshid, E. Villa, C. Chipot, R.D. Skeel, L. Kalé, K. Schulten, Scalable molecular dynamics with NAMD, *J. Comput. Chem.* 26 (2005) 1781–1802.
- [39] A.D. MacKerell Jr., N. Banavali, N. Foloppe, Development and current status of the CHARMM force field for nucleic acids, *Biopolymers* 56 (2000) 257–265.
- [40] T. Darden, D. York, L. Pedersen, Particle Mesh Ewald: an N³·log(N) method for Ewald sums in large systems, *J. Chem. Phys.* 98 (1993) 10089.
- [41] S.E. Feller, Y. Zhang, R.W. Pastor, B.R. Brooks, Constant pressure molecular dynamics simulation: the Langevin Piston method, *J. Chem. Phys.* 103 (1995) 4613–4621.
- [42] G.J. Martyna, D.J. Tobias, M.L. Klein, Constant pressure molecular dynamics algorithms, *J. Chem. Phys.* 101 (1994) 4177–4189.
- [43] S.A. Adelman, J.D. Doll, Generalized Langevin equation approach for atom/solid-surface scattering: general formulation for classical scattering off harmonic solids, *J. Chem. Phys.* 64 (2008) 2375–2388.
- [44] F. Zhu, E. Tajkhorshid, K. Schulten, Collective diffusion model for water permeation through microscopic channels, *Phys. Rev. Lett.* 93 (2004) 224501.
- [45] S. Henrich, O.M.H. Salo-Ahen, B. Huang, F.F. Rippmann, G. Cruciani, R.C. Wade, Computational approaches to identifying and characterizing protein binding sites for ligand design, *J. Mol. Recognit.* 23 (2010) 209–219.
- [46] F. Sirci, L. Goracci, D. Rodríguez, J. van Muijlwijk-Koezen, H. Gutiérrez-de-Terán, R. Mannhold, Ligand-, structure- and pharmacophore-based molecular fingerprints: a case study on adenosine A(1), A (2A), A (2B), and A (3) receptor antagonists, *J. Comput. Aided Mol. Des.* 26 (2012) 1247–1266.
- [47] L. Siragusa, S. Cross, M. Baroni, L. Goracci, G. Cruciani, BioGPS: navigating biological space to predict polypharmacology, off-targeting, and selectivity, *Proteins* 83 (2015) 517–532.
- [48] A.C. Cheng, R.G. Coleman, K.T. Smyth, Q. Cao, P. Soulard, D.R. Caffrey, A.C. Salzberg, E.S. Huang, Structure-based maximal affinity model predicts small-molecule druggability, *Nat. Biotechnol.* 25 (2007) 71–75.
- [49] G. Cruciani, M. Pastor, W. Guba, VolSurf: a new tool for the pharmacokinetic optimization of lead compounds, *Eur. J. Pharm. Sci. Off. J. Eur. Fed. Pharm. Sci.* 11 (Suppl. 2) (2000) S29–S39.
- [50] F. Milletti, L. Stocchi, G. Sforna, G. Cruciani, New and original pKa prediction method using grid molecular interaction fields, *J. Chem. Inf. Model.* 47 (2007) 2172–2181.
- [51] S. Pricl, M. Fermeglia, M. Ferrone, E. Tamborini, T315I-mutated Bcr–Abl in chronic myeloid leukemia and imatinib: insights from a computational study, *Mol. Cancer Ther.* 4 (2005) 1167–1174.
- [52] K. Miyazaki, Y. Abe, H. Iwanari, Y. Suzuki, T. Kikuchi, T. Ito, J. Kato, O. Kusano-Arai, T. Takahashi, S. Nishiyama, H. Ikeshima-Kataoka, S. Tsuji, T. Arimitsu, Y. Kato, T. Sakihama, Y. Toyama, K. Fujihara, T. Hamakubo, M. Yasui, Establishment of monoclonal antibodies against the extracellular domain that block binding of NMO-IgG to AQP4, *J. Neuroimmunol.* 260 (2013) 107–116.
- [53] A.S. Verkman, M.O. Anderson, M.C. Papadopoulos, Aquaporins: important but elusive drug targets, *Nat. Rev. Drug Discov.* 13 (2014) 259–277.
- [54] P.J. Hajduk, J.R. Huth, C. Tse, Predicting protein druggability, *Drug Discov. Today* 10 (2005) 1675–1682.
- [55] J. Owens, Determining druggability, *Nat. Rev. Drug Discov.* 6 (2007) 187.
- [56] L. Tradtrantip, H. Zhang, M.O. Anderson, S. Saadoun, P.-W. Phuan, M.C. Papadopoulos, J.L. Bennett, A.S. Verkman, Small-molecule inhibitors of NMO-IgG binding to aquaporin-4 reduce astrocyte cytotoxicity in neuromyelitis optica, *FASEB J. Off. Publ. Fed. Am. Soc. Exp. Biol.* 26 (2012) 2197–2208.
- [57] D. Seeliger, C. Zapater, D. Krenc, R. Haddoub, S. Flitsch, E. Beitz, J. Cerdà, B.L. de Groot, Discovery of novel human aquaporin-1 blockers, *ACS Chem. Biol.* 8 (2013) 249–256.